

# Oxide spinels with superior Mg conductivity

Mohsen Sotoudeh,<sup>\*,†</sup> Manuel Dillenz,<sup>†</sup> Johannes Döhn,<sup>†</sup> Julian Hansen,<sup>‡</sup> Sonia Dsoke,<sup>‡</sup> and Axel Groß<sup>\*,†,¶</sup>

<sup>†</sup>*Institute of Theoretical Chemistry, Ulm University, Oberberghof 7, 89081 Ulm, Germany*

<sup>‡</sup>*Institute for Applied Materials, Karlsruhe Institute of Technology,  
Hermann-von-Helmholtz-Platz 1, 76344 Eggenstein-Leopoldshafen, Germany*

<sup>¶</sup>*Helmholtz Institute Ulm (HIU) for Electrochemical Energy Storage, Helmholtzstraße 11,  
89069 Ulm, Germany*

E-mail: mohsen.sotoudeh@uni-ulm.de; axel.gross@uni-ulm.de

## Abstract

Mg batteries with oxide cathodes have the potential to significantly surpass existing Li-ion technologies in terms of sustainability, abundance, and energy density. However, Mg intercalation at the cathode is often severely hampered by the sluggish kinetics of  $\text{Mg}^{2+}$  migration within oxides. Here we report a combined theoretical and experimental study addressing routes to identify cathode materials with an improved Mg-ion mobility. Using periodic density functional theory calculations,  $\text{Mg}^{2+}$  migration in oxide spinels has been studied, revealing key features that influence the activation energy for  $\text{Mg}^{2+}$  migration. Furthermore, the electronic and geometrical properties of the oxide spinels as well as their stability have been analyzed for a series of different transition metals in the spinels. We find that electronegative transition metals enable a high Mg-ion mobility in the oxide spinel frameworks and thus a favorable cathode functionality. Based on the theoretical findings, some promising candidates have been identified, prepared and structurally characterized. Our combined theoretical and experimental findings open up an avenue toward the utilization of functional cathode materials with improved  $\text{Mg}^{2+}$  transport properties for Mg-metal batteries.

## Keywords

ionic conductivity, density functional theory, magnesium batteries, ternary oxide spinels

# Introduction

The field of post-lithium-ion batteries using, e.g., Na-ions<sup>1,2</sup> or Mg-ions<sup>3-6</sup> has recently received substantial attention in the quest for more sustainable and abundant batteries without compromising performance parameters such as energy density and capacity. In particular the concept of pairing a metallic anode with a high voltage cathode promises to achieve higher energy density<sup>7,8</sup> than current Li-ion technologies. Among them, batteries based on the bivalent metal magnesium theoretically reach higher volumetric energy densities compared to monovalent-based batteries.<sup>7,8</sup> However, among the materials typically used in Mg batteries only few combine an acceptable ionic conductivity with a high operating voltage. For example,  $\text{MgMo}_6\text{S}_8$ <sup>4</sup> and  $\text{MgTi}_2\text{S}_4$ <sup>9</sup> sulfides allow an effective reversible Mg intercalation. Still, their capacities and operation potentials are too low to enable devices with a competitive energy density.

In contrast to materials based on soft anions such as sulfides, oxide materials combined with a metallic Mg anode offer high voltages and capacities.<sup>10</sup> As an example, the ion-exchanged olivine-type  $\text{MgFeSiO}_4$  cathode exhibits a relatively high potential of 2.4 V vs.  $\text{Mg}^{2+}/\text{Mg}$  and a capacity of 300 mAh/g.<sup>11</sup> This material represents a low-cost, safe and corrosion free cathode which can be applied in rechargeable Mg batteries. Furthermore,  $\text{MgMnSiO}_4$  has been considered as a potential cathode candidate material for Mg batteries.<sup>12</sup> However, spinel structures typically show a lower migration barrier compared to the olivine structures. Finding spinel materials with a high ionic conductivity has therefore become an active topic of research in the field of Mg batteries.<sup>13-20</sup>

As already mentioned above, inorganic oxides in the spinel structure<sup>14,21</sup> exhibit a favorable combination of capacity and voltage, as illustrated in Fig 1. Recently, experimental  $\text{Mg}^{2+}$  migration barriers of about 600 meV have been reported in Cr- and Mn-spinel oxides, in agreement with density functional theory (DFT) calculations.<sup>21</sup> It has been found that Mg-ion migration is influenced by structural disorder in the spinel lattice, which can be controlled during synthesis.<sup>21</sup> However, the strong Coulombic interactions of the Mg cations

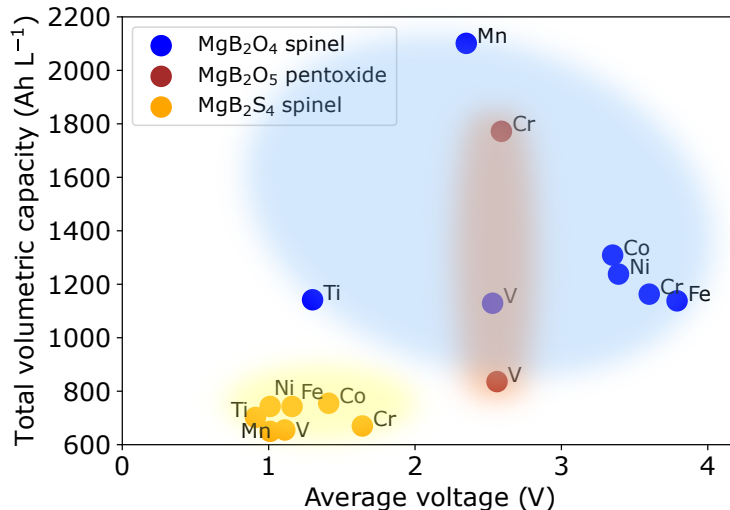


Figure 1: Total volumetric capacity versus average voltage for MgB<sub>2</sub>S<sub>4</sub> sulfide spinels (orange), MgB<sub>2</sub>O<sub>4</sub> oxide spinels (blue) as well as MgB<sub>2</sub>O<sub>5</sub> pentoxides (brown), derived from DFT calculations within the PBE+*U* approach. The colored areas represent the estimated range of the corresponding compounds.

with the oxide host lattice generally hamper the reversibility of Mg intercalation and lead to high Mg migration barriers.<sup>22</sup> Recently, we have been able to identify a descriptor for the ion mobility in crystalline materials based on the ionic radii, the oxidation states and the difference in the electronegativities of the migrating cations and the anions of the host lattice.<sup>19</sup> Furthermore, we explored the effect of the transition metal cations in spinel compounds on their transport properties, suggesting that the transition metals can significantly influence the Mg<sup>2+</sup> migration barriers in these compounds.<sup>19,20</sup> Applying this concept, we found that oxide spinels combined with large electronegative transition metal cations promise to exhibit a rather high Mg<sup>2+</sup> mobility.<sup>19</sup>

It should be mentioned that utilizing *4d* and *5d* transition metals instead of *3d* transition metals can lead theoretically to high capacity electrode materials for rechargeable batteries.<sup>23,24</sup> The *4d* and *5d* transition metals had been overlooked for a long time due to their unfavorable weight. However, employing anionic redox mechanisms can enable large reversible capacities.<sup>25</sup> As an example, the rock salt compound Li<sub>1.3</sub>Nb<sub>0.3</sub>Mn<sub>0.4</sub>O<sub>2</sub> with the *4d* transition metal Nb was found to exhibit a high reversible capacity of 300 mAh g<sup>-1</sup> in Li-ion

batteries.<sup>23</sup> Even for chalcogenide spinel lattices, it was recently shown that their Mg-ion mobility can be enhanced by selecting the heavy transition metal lanthanoid.<sup>24</sup> Therefore, the use of  $4d$  and  $5d$  transition metals in cathode materials can not only lead to high voltages but also to promising ion mobilities.

In this work, based on our descriptor concept for the ion mobility,<sup>19</sup> we will take the next step towards the realisation of battery materials with improved migration properties. Performing electronic first-principles density functional theory (DFT) calculations, we focus on  $3d$  oxide spinels and their  $\text{Mg}^{2+}$  mobility by considering  $4d$  and  $5d$  metals as dopants in our calculations in order to improve the properties of the spinels. Based on the theoretical results, the synthesis of materials with predicted improved properties was initiated, leading to the synthesis of promising cathode materials at different doping levels. As the next step, the properties of these materials as battery cathodes will be experimentally tested. This work thus reports the first steps in the identification and utilization of promising battery materials based on an understanding of the fundamental principles underlying battery operation at the atomic level.

## Methods

### Computational details

First-principles calculations in the framework of density-functional theory (DFT)<sup>26–28</sup> were performed for  $\text{MgB}_2\text{O}_4$  spinel structures. The exchange-correlation effects were described in the generalized gradient approximation (GGA) using the Perdew-Burke-Ernzerhof (PBE) functional.<sup>29</sup> The calculations were carried out with the Projector Augmented Wave (PAW)<sup>30</sup> method as implemented in the Vienna *Ab-initio* Simulation Package.<sup>31–33</sup> The PAW pseudopotentials include the  $2p$  and  $3s$  orbitals of Mg, the  $2s$ ,  $2p$  of O, the  $3d$ ,  $4s$  orbitals of Ti, Co, Ir, and the  $3p$ ,  $3d$ ,  $4s$  orbitals for other transition metals.

A plane wave cutoff of 520 eV has been chosen for the wave function, and the convergence

criterion for total energies was set to  $1 \times 10^{-5}$  eV per supercell. A  $2 \times 2 \times 2$  k-point mesh has been used for the unit cell containing eight formula units with 56 atoms. The partial occupancies for each orbital are set with the tetrahedron method<sup>34,35</sup> and the so-called Blöchl corrections.<sup>36</sup> The atomic positions and volume are relaxed without any restriction.

In the simulations, to properly describe the localized (strongly correlated)  $d$ -electrons, Hubbard  $U$  corrections<sup>37</sup> have been used. For the  $3d$  orbitals of the transition metals, they have been set to  $U_{\text{Ti}} = 3.00$  eV,  $U_{\text{V}} = 3.25$  eV,  $U_{\text{Cr}} = 3.70$  eV,  $U_{\text{Mn}} = 3.90$  eV,  $U_{\text{Fe}} = 5.30$  eV,  $U_{\text{Co}} = 3.32$  eV, and  $U_{\text{Ni}} = 6.20$  eV. For Ir and Rh, only the conventional GGA-PBE functional is used without any  $U$  parameter.

The electronic structure in oxide spinels strongly depends on the type of magnetic order in the material. Both antiferromagnetic and ferromagnetic orders are probed to identify the ground state of the systems. Our calculations show that in general the ferromagnetic structures are energetically less stable than the antiferromagnetic configurations that have a zero overall magnetic moment for the  $3d$  transition metals. Thus, the electronic structure has been set to collinear antiferromagnetic spin arrangements for  $3d$  transition metals, while for Co, Rh, and Ir metals, a non-magnetic order has been assumed.

In order to identify the Mg-ion migration barriers, the nudged elastic band (NEB)<sup>38</sup> method was used. In order to model the Mg migration, one Mg atom was removed within the supercell, resulting in a  $\text{Mg}_{0.875}\text{B}_2\text{O}_4$  stoichiometry. It should be noted that the diffusion in the considered compounds is referred to as interstitial diffusion in the literature.<sup>39</sup> During the NEB calculations, the total energies were evaluated with the PBE functional and PBE+ $U$  corrections in order to validate the calculated migration barrier energies. All of the NEB calculations have been carried out with four distinct images between the tetrahedral and octahedral sites to evaluate the Mg-ion migration trajectory. The NEB calculations were fully relaxed until the forces on the atoms were converged within  $0.05 \text{ eV } \text{Å}^{-1}$ . As Fig. 2 demonstrates, including  $U$  corrections severely alters the calculated migration barrier heights, for early transition metals the barriers are increased by up to 0.5 eV, whereas

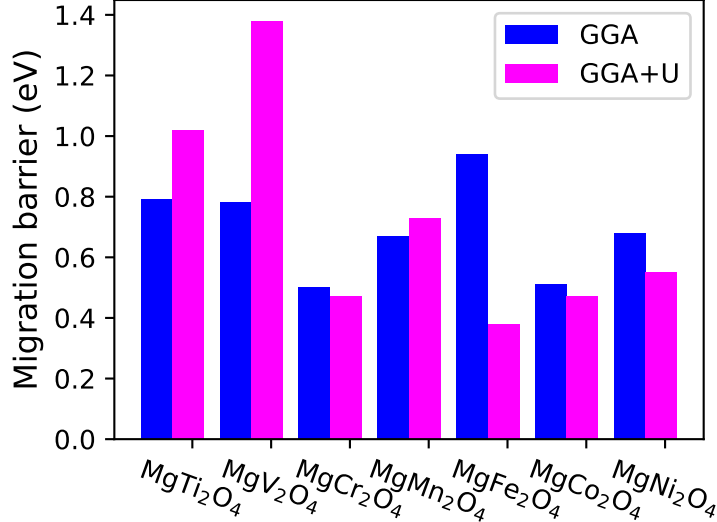


Figure 2: Calculated migration barrier energies using the PBE and PBE+ $U$  functionals for the 3d transition metal oxides in the spinel framework.

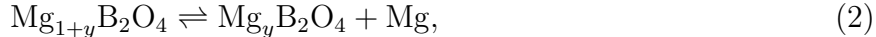
for the late transition metals, decreased by up to 0.5 eV. We consider the migration barriers determined with the  $U$  correction to be less reliable for the following reasons: despite the correct prediction of the ground state configurations, including all distortions, the PBE+ $U$  functionals provide inaccurate energy differences between the tetrahedral site and octahedral void, namely inaccurate site preference energies, as demonstrated by comparing DFT+ $U$  calculations with DFT calculations including exact exchange. For example the site preference energy in the MgV<sub>2</sub>O<sub>4</sub> is about 0.7 eV using the PBE functional and about 0.5 eV using the HSE06 functional,<sup>40</sup> while the PBE+ $U$  functional yields an energy of about -0.1 eV. Therefore, obviously the PBE functional yields a better estimate of the migration barrier energy for the considered materials in the present work than the PBE+ $U$  functional.

The open circuit voltage ( $V_{OC}$ ) of the spinel materials is given by

$$V_{OC} = -\frac{E_{inter}}{zFx}, \quad (1)$$

where  $F$  is the Faraday constant, and  $z$  corresponds to the elementary charges that are

transferred between anode and cathode upon the process



with  $z = 2$  for Mg-ion batteries.  $E_{inter}$  is the Mg intercalation energy in the spinel structure with respect to metallic magnesium which has been calculated, neglecting the zero-point energies and entropic contributions, according to

$$E_{inter}(\text{Mg}) = E(\text{Mg}_{1+y}\text{B}_2\text{X}_4) - (E(\text{Mg}_y\text{B}_2\text{X}_4) + xE(\text{Mg})) , \quad (3)$$

where  $E(\text{Mg}_y\text{B}_2\text{X}_4)$  is the total energy of the spinel with a Mg concentration  $y$  in the unit cell, and  $E(\text{Mg})$  is the cohesive energy of Mg bulk metal. The open circuit voltage  $V_{OC}$  in volts is given by  $E_{inter}/2$  for Mg-metal batteries when  $E_{inter}$  is given in eV.

Thermodynamic stability has been used to address the theoretical chemical stability and synthesizability,<sup>41</sup> comparing a compound’s energy with all possible configurations with the same stoichiometry. The existing Materials Project<sup>42</sup> databases have been utilized to evaluate all possible decomposition products. The difference to the configuration with the lowest energy, commonly termed as the energy above hull  $E_{hull}$ , is provided here as a measure for stability. In order to correctly calculate  $E_{hull}$ , the following procedures have been taken into account: i) We have carefully checked that the formation energies of all considered compounds agree well with the corresponding values given by the Materials Project. ii) The well-known problems due to the overbinding of dioxygen in GGA calculations are accounted by a correction suggested by Wang et al.<sup>43</sup> iii) We do not consider the decomposition of the considered compounds into elemental metals, preventing the problem of comparing the GGA+U energies of the oxide phases with the GGA calculations of the elemental metallic phases.<sup>44</sup> In the discussion of the stability of the considered structures given below we consider structures to be stable if their energy above hull is below 0.05 eV/atom, first of all due to the fact that the accuracy of our DFT calculations is in this range, and second, because



structures that are only slightly unstable with respect to the thermodynamically most stable structure might still be kinetically rather stable.

## Results and Discussion

### Spinel structure

The oxide spinel structure which the chemical formula  $AB_2O_4$  crystallizes with a cubic close-packed oxygen lattice. In the normal spinel crystal structure, A cations occupy 1/8 of the tetrahedral sites, while B cations fill 1/2 of the octahedral sites as shown in Fig. 3a. B and O ions form a network of edge-sharing  $BO_6$  octahedra, whereas A and O ions form a three-dimensional network of corner-sharing tetrahedra. In the oxides studied here, the size of the A-type ions is sufficiently small making their occupation of the tetrahedral site energetically more preferable than the occupation of the octahedral sites.<sup>18</sup> The network made by the B ions is known as the pyrochlore lattice, as shown in Fig. 3b. The pyrochlore lattice gives rise to very strong geometrical frustration effects. Two types of alternate stacking planes, namely a two-dimensional triangular and a kagomé lattice, can form along the [111] direction, as shown in Fig. 3c. The A sublattice of the spinel structure assumes the shape of a diamond lattice, which is shown in Fig. 3d. The presence of several competing factors, such as the crystal field stabilization of the transition metals (B cations) or entropic contributions, can result in a variety of disordered or inverted configurations.<sup>45</sup> A fraction of A cations (such as Mg) can change sites with the transition metal B cations, resulting in partially inverted lattices and charge disproportionation of the B cations ( $2B^{3+} \rightarrow B^{2+} + B^{4+}$ ).

Many spinel oxides have cubic symmetry at high temperatures, but this does not rule out the possibility of distorted  $BO_6$  octahedra. The octahedra undergo compression or elongation along the [111] direction, pointing towards the centers of the  $BO_4$  tetrahedra, as illustrated in Fig. 4. This gives rise to a trigonal distortion of the octahedra, changing the  $O_h$  octahedral symmetry to a  $D_{3h}$  octahedral symmetry.<sup>46</sup> The trigonal distortion can

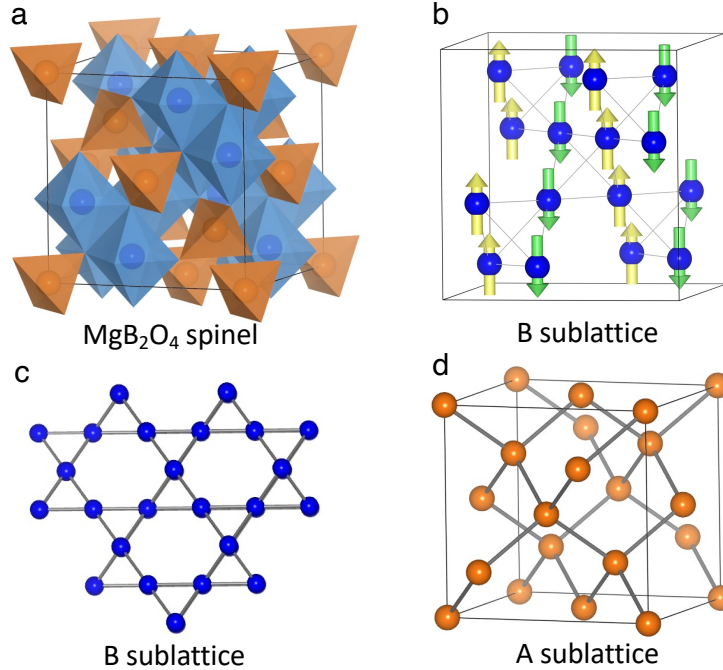


Figure 3: (a) Spinel structure, emphasizing the two basic structural units of  $\text{AO}_4$  tetrahedra and  $\text{BO}_6$  octahedra. (b) B sublattice of spinel structure, which defines a pyrochlore lattice, and the lowest-energy spin states obtained by PBE+ $U$ . The B-cations are colored in blue. Green and yellow arrows represent the two spin directions. (c) B-sublattice structure (pyrochlore lattice) viewed from the  $\langle 111 \rangle$  direction. (d) A sublattice (diamond lattice).

be parameterized by the anion parameter  $u$ <sup>47</sup> which reflects the displacement of the O-ions within the cubic cell. In ideal octahedra  $u = 3/8$ , whereas  $u < 0.375$  indicates a compression of the octahedra and  $u > 0.375$  corresponds to their elongation. Sickafus et al.<sup>47</sup> showed that the anion parameter  $u$  can be expressed as a function of the effective radii  $r$  of Mg and of the transition metal B according to

$$u = 0.3876 \left( \frac{r(\text{B})}{r(\text{Mg})} \right)^{-0.07054}. \quad (4)$$

This distortion is an important factor influencing the electronic configuration of the transition metals in the spinel structure. The resulting values for the considered oxide spinels are given in Tab. 1. All compounds show  $u$  values higher than 0.375 confirming the existence of trigonal distortion for all cases.

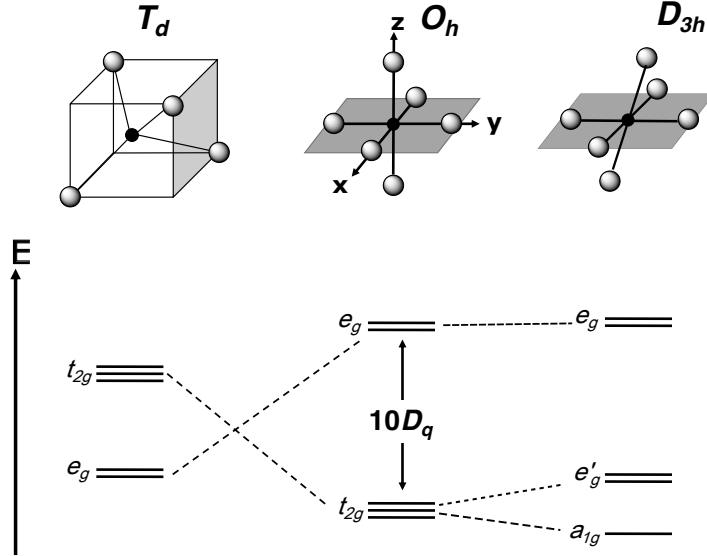


Figure 4: Schematic representation of the crystal field splitting of  $d$ -orbitals at a tetrahedral site ( $T_d$ ) and at octahedral sites without ( $O_h$ ) and with the trigonal distortion ( $D_{3h}$ ). The central B cation is assumed to be coordinated by oxygen atoms.

Table 1: Calculated anion parameter  $u$  indicating the local trigonal distortion of the  $\text{BO}_6$  octahedra, using Eq. 4 and the oxygen radius of 1.36 Å. The ionic radii of the B cations are taken from Shannon<sup>48</sup> for a sixfold coordinated configuration and the corresponding ionic charge of 3+ present in this list.

Compound	$r(\text{B})/\text{Å}$	Anion parameter
$\text{MgTi}_2\text{O}_4$	0.67	0.4074
$\text{MgV}_2\text{O}_4$	0.64	0.4088
$\text{MgCr}_2\text{O}_4$	0.62	0.4097
$\text{MgMn}_2\text{O}_4$	0.65	0.4083
$\text{MgFe}_2\text{O}_4$	0.65	0.4083
$\text{MgCo}_2\text{O}_4$	0.61	0.4102
$\text{MgNi}_2\text{O}_4$	0.60	0.4106
$\text{MgIr}_2\text{O}_4$	0.67	0.4074
$\text{MgRh}_2\text{O}_4$	0.68	0.4070

## Basic electronic configuration

In Fig. 5, we have plotted the calculated density of states whose gross features we will now summarize. Most spinel oxides containing  $d$ -series transition-metal ions exhibit magnetic insulator configurations due to the strong Coulomb repulsion within the  $d$ -orbitals. In rare

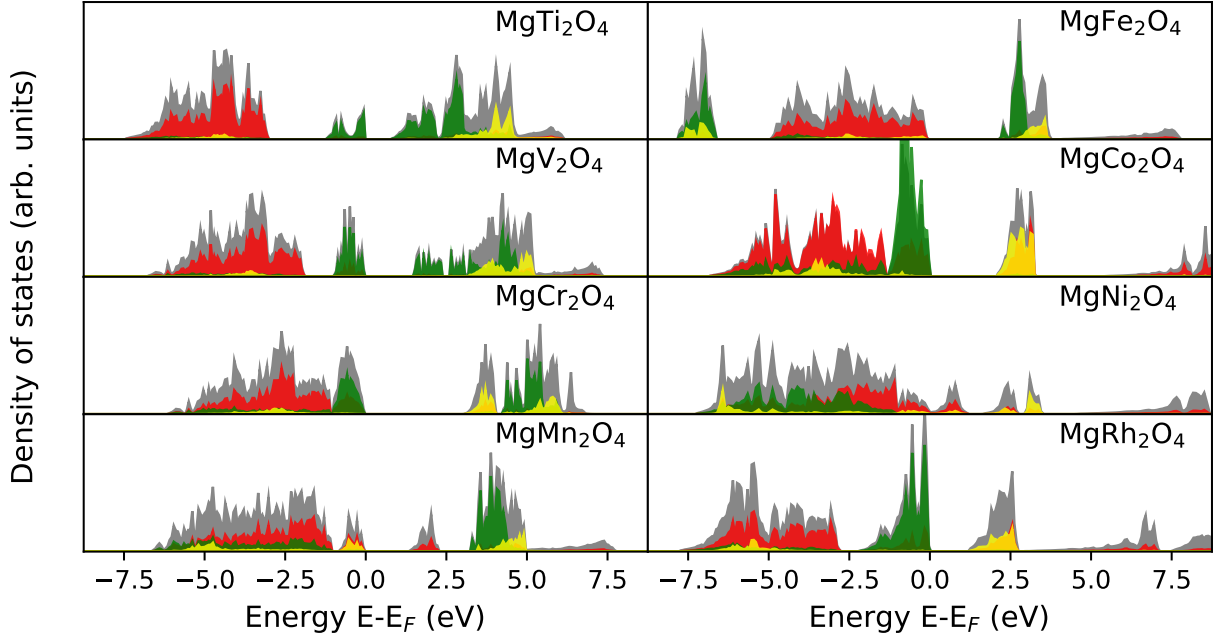


Figure 5: DOS of  $\text{MgM}_2\text{O}_4$  ( $B = \text{Ti, V, Cr, Mn, Fe, Co, Ni, and Rh}$ ) spinel structures in the stable antiferromagnetic order for  $3d$  metals and non-magnetic order for Rh. The graphs show the total DOS (grey) and the projected DOS for O- $p$  (red), B- $t_{2g}$  (green), B- $e_g$  (yellow). The projected DOS is considered for the B ions with both majority- and minority-spin directions.

cases, a spin-singlet state forms, and the system tends to be non-magnetic. Compared to sulfide spinels, oxides are less conducting due to their decreased bandwidth, which weakens  $p$ - $d$  hybridization.<sup>49</sup>

Crystal field splitting divides the transition-metal  $d$ -orbitals, located at the B site of a regular  $\text{BO}_6$  octahedron, into high-lying, doubly degenerate  $e_g$  and low-lying triply degenerate  $t_{2g}$  orbitals, as illustrated in Fig. 4. Note that the crystal-field splitting originates from the covalent interaction with the oxygen neighbors. The stronger  $\sigma$  bond of the  $e_g$  states in comparison to the  $\pi$  bonds formed by the  $t_{2g}$  states shifts the antibonding  $e_g$  states energetically above the  $t_{2g}$  states. In addition to the crystal field splitting, the local trigonal distortion further divides the  $t_{2g}$  orbitals into an  $a_{1g}$  orbital, and doubly degenerate  $e'_g$  orbitals. At low temperatures, alternatively a tetragonal distortion splits the  $t_{2g}$  orbitals into  $xy$  and the doubly degenerate  $yz/zx$  pair and the doubly degenerate  $e_g$  orbitals into

non-degenerate  $x^2 - y^2$  and  $3z^2 - r^2$  orbitals.

If a transition-metal ion locates in the tetrahedral A site, the transition-metal  $d$ -orbitals split into the high-lying  $t_{2g}$  and low-lying  $e_g$  orbitals, opposite to the octahedral B-site. The B-ions in spinels usually have a large magnetic moment, leading to a Hund's rule-splitting between transition-metal  $d$  levels in the majority and the minority spin direction and changes in orbital character.

## Jahn-Teller distortions

In continuation of the preceding considerations, we now further analyze the different electronic configurations occurring in oxide spinels. The local structure around the transition metal ion will be affected by the electron filling of the  $3d$ -orbitals, namely the Jahn-Teller effect. A prominent Jahn-Teller configuration is  $3t_{2g}^3e_g^1$  ( $\text{Mn}^{3+}$ ). The high-spin configuration of the  $\text{Mn}^{3+}$  ion introduces a single electron in the  $\text{Mn-}e_g$  state. The system lowers its energy through a tetragonal distortion which splits the doubly degenerate  $e_g$  level into the singly filled  $d_{3z^2-r^2}$  orbital and the higher lying empty  $d_{x^2-y^2}$  orbital. In contrast, for  $d^3$  and  $d^5$  configurations, the  $e_g$  states are either empty or filled, respectively, and therefore, no Jahn-Teller distortion occurs. The 3-fold degenerate  $t_{2g}$ -states form metal-oxygen  $\pi$ -bonds, which are weaker than the  $e_g$   $\sigma$ -bonds, and therefore, the Jahn-Teller effect is smaller compared to the  $e_g$ -states. Hence, weak distortions are expected for  $3d^1$  ( $\text{Ti}^{3+}$ ),  $3d^2$  ( $\text{V}^{3+}$ ), and  $3d^3$  ( $\text{Cr}^{3+}$ ) as well as the  $3t_{2g}^4e_g^2$  ( $\text{Co}^{3+}$ ) and  $3t_{2g}^5e_g^2$  ( $\text{Ni}^{3+}$ ) configuration. The Rh- and Ir-spinels show no Jahn-Teller distortions due to the predominant ferromagnetic order of these spinels which enhances the  $p$ - $d$  hybridization.

## Selected oxide spinels

After reviewing the gross features of the atomic and the electronic structure of the oxide spinels, we will now discuss how transition metals affect the Mg migration in the series of magnesium oxide spinels considered in this study. We concentrate on normal spinel phases

that crystallize in cubic single-phase lattices (space group  $Fd\bar{3}m$ , see Fig. 3).

### **MgTi<sub>2</sub>O<sub>4</sub>**

The first member of the class of oxide spinels considered in this study is MgTi<sub>2</sub>O<sub>4</sub>. The ions are in the formal oxidation states Mg<sup>2+</sup>Ti<sub>2</sub><sup>3+</sup>O<sub>4</sub><sup>2-</sup>. Thus, an electron is inserted into the  $t_{2g}$  states of the Ti sites. The  $3d^1$  electronic configuration together with the total spin  $S = 1/2$  make this system to a strong candidate for the occurrence of dimerization in a single-valence system. In fact, MgTi<sub>2</sub>O<sub>4</sub> undergoes a metal-insulator (M-I) transition when cooled below  $T_{M-I} = 260$  K, accompanied by a strong decrease of the magnetic susceptibility and a transition to a tetragonal structure. In the tetragonal structure of MgTi<sub>2</sub>O<sub>4</sub>, Ti moves away from the center of the TiO<sub>6</sub> octahedron, and the six nearest-neighbor Ti-Ti distances become inequivalent.

The calculated DOS of MgTi<sub>2</sub>O<sub>4</sub> is shown in Fig. 5. The filled valence band, which extends from -7 eV to 0 eV, consists of predominantly O- $p$  character from -7 eV to -3V with some contribution of Ti- $d$  orbitals from -1 eV to 0 eV. The unfilled Ti- $d$  states are located 1-5 eV above the valence band. The Ti-based spinel has the lowest voltage with respect to a Mg metal anode among all the Mg spinel compounds based on other redox-active cations. The Ti-based compound has an energy of 0.013 eV/atom above *hull* which shows the stability of the compound and the possibility to be synthesized. Compared to an ideal octahedron that possesses Ti-O distances with equal length, two Ti-O bonds are compressed by 6% in this system. Thus, the octahedron has both tetragonal and trigonal distortions, within the corresponding point group  $D_{3h}$ .

The Ti oxide spinel is associated with a low open-circuit voltage with respect to magnesium metal as well as rather high Mg migration barrier, i.e. a low ion mobility, as detailed in Tab. 2. The inverse spinel, Mg<sub>2</sub>TiO<sub>4</sub>, is more stable, which makes Mg-ion migration even more difficult. Thus this compound is not suited as a cathode material for Mg batteries.

Table 2: Mg-O, and B-O bond lengths in Å for spinel compounds. B denotes the transition-metal. Calculated relative barrier energy  $E_a$ , energy above hull  $E_{hull}$ , intercalation energy  $E_{inter}^{high}$  ( $E_{inter}^{low}$ ) (Eq. 3) for high (low) Mg concentration in eV, and corresponding open-circuit voltage  $V_{OC}^{high}$  ( $V_{OC}^{low}$ ) with respect to a Mg metal anode in V. The volume changes with respect to the structure without Mg is indicated by  $\Delta V/V$ .

Compound	Mg-O (Å)	B-O (Å)	$E_a^{PBE}$ (eV)	$E_{hull}$ (eV/atom)	$E_{inter}^{high}$ (eV)	$V_{OC}^{high}$ (V)	$E_{inter}^{low}$ (eV)	$V_{OC}^{low}$ (V)	$\Delta V/V$ (%)
MgTi <sub>2</sub> O <sub>4</sub>	2.027	2.025/2.147	0.791	0.013	-2.258	1.129	-3.805	1.903	-3.5
MgV <sub>2</sub> O <sub>4</sub>	1.993	2.040/2.072	0.783	0.013	-5.464	2.732	-5.090	2.545	-1.4
MgCr <sub>2</sub> O <sub>4</sub>	1.994	2.031/2.033	0.497	0.037	-7.318	3.659	-6.994	3.497	-1.5
MgMn <sub>2</sub> O <sub>4</sub>	1.998	1.961/2.312	0.672	0.036	-5.958	2.979	-4.817	2.409	-0.9
MgFe <sub>2</sub> O <sub>4</sub>	2.002	2.049/2.053	0.940	0.000	-7.696	3.848	-6.959	3.479	0.8
MgCo <sub>2</sub> O <sub>4</sub>	1.965	1.931	0.513	0.039	-6.754	3.377	-8.688	4.344	3.2
MgNi <sub>2</sub> O <sub>4</sub>	1.973	1.878/2.030	0.680	0.064	-7.188	3.594	-4.311	2.155	-2.0
MgIr <sub>2</sub> O <sub>4</sub>	2.064	2.096	0.319	0.287	-3.956	1.978	-4.557	2.278	3.6
MgRh <sub>2</sub> O <sub>4</sub>	2.027	2.069	0.429	0.000	-4.390	2.195	-5.871	2.935	2.4

## MgV<sub>2</sub>O<sub>4</sub>

Passing from MgTi<sub>2</sub>O<sub>4</sub> to MgV<sub>2</sub>O<sub>4</sub>, the octahedral site is now filled by V<sup>3+</sup> which accommodates two electrons into the triply degenerate  $t_{2g}$  orbitals. The orbital degrees of freedom of these electrons allow a more complex interplay of frustrated spins and orbitals. The trigonal distortion plays a significant role in this compound while the tetragonal distortion is not pronounced. The Vi-O bonds are compressed by 1%, splitting the  $t_{2g}$  orbitals.

MgV<sub>2</sub>O<sub>4</sub> is a S = 1 Mott insulator with a pyrochlore lattice. The DOS of MgV<sub>2</sub>O<sub>4</sub> shown in Fig. 5 reveals that filled V- $d$  states are located above the oxygen valence band in the range from -1 eV to 0 eV. The empty V- $d$  states are located in the range from 1.5 eV to 6 eV. Compared to the Ti spinel, the  $t_{2g}$  orbitals are filled to a larger degree and are shifted downward close to the O- $p$  states. Similar to the Ti spinel, this compound has an energy of 0.013 eV/atom above *hull* indicating that this material could be synthesized and it may be stable.

As Tab. 2 shows, the calculated open-circuit voltage for the V spinel is about 2.7 V, however, the height of the migration barrier for Mg is 0.783 eV, indicative of a low ion mobility. The normal spinel, MgV<sub>2</sub>O<sub>4</sub>, is more stable than the inverse one. However, inspite of the high potential, the low ion mobility prohibits the use of this compound as cathode

material.

### **MgCr<sub>2</sub>O<sub>4</sub>**

MgCr<sub>2</sub>O<sub>4</sub> is an  $S = 3/2$  Mott insulator with trivalent Cr. The three electrons are accommodated in the triply degenerate  $t_{2g}$  orbitals of Cr- $d$ , which all three degenerate states singly occupied, and cooperative distortions of the CrO<sub>6</sub> octahedra are absent with no orbital degrees of freedom. This compound exhibits a geometrical frustration associated with the pyrochlore structure of the Cr-sublattice.

The calculated DOS of MgCr<sub>2</sub>O<sub>4</sub> shown in Fig. 5 exhibits filled Cr- $t_{2g}$  orbitals located in the upper part of the O- $p$  band in the range from -1 eV to 0 eV. In contrast to the Ti and V spinels, the filled  $t_{2g}$  orbitals are merged with the upper part of the oxygen valence band. The bottom part of the conduction band consists of Cr- $e_g$  orbitals in the majority spin orientation. Structurally the Cr-O bonds are almost equal in the CrO<sub>6</sub> octahedra, and solely trigonal distortions play a role. This compound has an energy above *hull* of 0.037 eV/atom which indicates that the structure is possibly stable. Compared to the other  $3d$  oxide spinel, it has relatively small Mg migration barriers.

The small migration barrier of 0.497 eV and open-circuit voltage of 3.6 V demonstrate that this compound can potentially be used as a cathode material (see Tab. 2). The reported experimental value of  $0.62 \pm 0.10$  eV for the Mg migration barrier in MgCr<sub>2</sub>O<sub>4</sub> at high temperature<sup>21</sup> is consistent with our calculation.

### **MgMn<sub>2</sub>O<sub>4</sub>**

MgMn<sub>2</sub>O<sub>4</sub> is an  $S = 2$  Mott insulator with four electrons in the Mn- $d$  orbitals. The  $t_{2g}$  orbitals are filled by three electrons, and an additional electron is inserted into the anti-bonding  $e_g$  states of the Mn sites. The presence of the electron in the  $e_g$  orbitals causes the formation of Jahn-Teller polarons. Structurally, two Mn-O bonds in the MnO<sub>6</sub> octahedra are elongated by 18% and cause a splitting of the doubly degenerate  $e_g$  orbitals. Thus,



the bandgap in  $\text{MgMn}_2\text{O}_4$  is affected by this Jahn-Teller effect. Note that the weakening of the Mn-O antibonding orbitals with neighboring oxygen atoms upon the increase of the corresponding Mn-O bond distances causes a stabilization of the occupied states.

As shown in Fig. 5, the filled valence band in  $\text{MgMn}_2\text{O}_4$ , which extends from -6 eV to 0 eV, is predominantly of O- $p$  character with some contribution from the Mn- $d$  orbitals. The filled Mn- $e_g$  states in the majority spin directions are located in the upper part of the oxygen valence band in the range from -1 eV to 0 eV. The empty Mn- $e_g$  states in the majority spin direction are in the range from 1.5 eV to 2 eV. In this compound, both tetragonal and trigonal distortions play a significant role. The energy above *hull* of 0.036 eV/atom indicates possible stability of the structure.

Furthermore, we obtained a migration barrier of 0.672 eV in agreement with the experimental value of  $0.690 \pm 0.090$  eV.<sup>21</sup> Still, compared to the other  $3d$  oxide spinel, this only allows a relatively low mobility for the Mg ions due to the high migration barrier. The open-circuit voltage is 2.98 V. Nonetheless, the rather low stability makes the formation of the Mg-Mn antisite defects upon inversion and consequently an even larger migration barrier very likely. It should be mentioned that  $\text{MgMn}_2\text{O}_4$  stabilizes in the tetragonal crystal structure at low temperature. Thus a phase transition occurs from the cubic structure to the tetragonal one. Still, compared to the other  $3d$  oxide spinel, the Mn spinel shows relatively high voltage and stability, which makes it a potential candidate for cathode usage.

### **MgFe<sub>2</sub>O<sub>4</sub>**

$\text{MgFe}_2\text{O}_4$  is an  $S = 5/2$  Mott insulator with half-filled Fe- $d$  orbitals. As  $\text{Fe}^{3+}$  accommodates five electrons in the  $d$  orbitals within the high spin configuration, this system exhibits a geometrical frustration of the Fe-sublattice with no orbital degree of freedom. The band gap lies between filled O- $p$  and the empty  $t_{2g}$  states on the Fe site in the minority-spin direction which determines all important features of the transport properties in the Fe-spinel. Structurally, the Fe-O bonds in the  $\text{FeO}_6$  octahedra are elongated by 0.5%, which,

however, causes no Jahn-Teller active mode due to the small distortion.

In contrast to the other  $3d$  spinel oxides, the top of the valence band has an O- $p$  character, and the Fe- $d$  orbitals in the majority spin direction split off below the O- $p$  valence band from -6.5 eV to -8 eV, as shown in Fig. 5. The conduction band consists of Fe- $d$  states in the minority-spin direction in the range of 2-4 eV. The bandgap is about 2 eV predominantly in majority-spin direction. All Fe-O bond lengths are equal showing that only trigonal distortions play a role in this compound. The small energy above *hull* of 0.000 eV/atom indicates a high stability which means that one should be able to prepare this material. However, this compound shows the highest Mg migration barrier and thus the lowest Mg-ion mobility compared to the other considered  $3d$  oxide spinels. Note that the Fe spinel lattice has a half-closed shell which presumably makes it challenging to remove electrons.

The Fe spinel possesses the highest open-circuit voltages among the considered oxide spinels, as detailed in Tab. 2. However, despite the high voltage, this compound suffers from low ion mobility.

### **MgCo<sub>2</sub>O<sub>4</sub>**

The Co spinel oxide is a non-magnetic Mott insulator in which its electrons in the Co- $d$ -orbitals are paired. This compound accommodates six electrons in the  $d$ -orbitals, introducing three electrons with opposite signs in the  $t_{2g}$  states. Thus, this system exhibits no geometrical frustration in the Co-sublattice, orbital, and spin degrees of freedom. Structurally, the Co-O bonds in the CoO<sub>6</sub> octahedra are identical, and only the trigonal distortion plays an important role.

The calculated DOS of MgCo<sub>2</sub>O<sub>4</sub> (see Fig. 5) shows a filled valence band which extends from -7 eV to 0 eV, predominantly of O- $p$  character with the filled contribution of Co- $t_{2g}$  orbitals in the upper part of the valence band. The conduction band dominantly consists of the empty Co- $e_g$  contributions along with oxygen bands. In this compound, the trigonal distortion is strong compared to the other considered oxide spinel and causes a broadening

of the Co- $t_{2g}$  orbitals.

This Co oxide exhibits a good ionic conductivity reflected in the relatively low Mg migration barrier of 0.513 eV, hence it might be a good candidate as a cathode material. The energy above *hull* of 0.039 eV/atom shows that the spinel framework is may be the stable phase for Co. The Co spinel shows a relatively high open-circuit voltage of 3.38 eV which makes it a promising candidate as electrode material. However, among the considered oxide spinels, this material has a relatively large volume change of 3% upon charging/discharging which is, however, still acceptable (see below).

### **MgNi<sub>2</sub>O<sub>4</sub>**

In contrast to the other normal spinels, MgNi<sub>2</sub>O<sub>4</sub> is weakly metallic with  $S = 3/2$ . This compound accommodates seven electrons in the  $d$ -orbitals, introducing two electrons in the minority-spin direction of the  $t_{2g}$  states. There is an interplay of frustrated spins and orbital degrees of freedom in this system. Structurally, two Ni-O bonds are elongated by 8% in the NiO<sub>6</sub> octahedra which leads to the presence of distortion modes.

The calculated DOS of MgNi<sub>2</sub>O<sub>4</sub> in Fig. 5 shows a continuously filled valence band from -7 eV to 0 eV, predominantly of O- $p$  and Ni- $d$  character. At the valence band top, the Ni- $t_{2g}$  state in the minority-spin direction splits into filled and empty orbitals with a small gap. Thus, the small bandgap in MgNi<sub>2</sub>O<sub>4</sub> is due to the splitting of Ni- $t_{2g}$  in the minority-spin direction. This compound shows a strong trigonal distortion compared to the other considered oxide spinel, but also tetragonal distortions play a role.

The energy above *hull* of 0.064 eV/atom indicates a low possibility for synthetization and stability of the material. However, this compound has a rather large Mg migration barrier indicating a low ionic conductivity. The calculated open-circuit voltage is about 3.6 eV, which is relatively high. Our calculations demonstrate a drop in potential to about 2.1 eV for low Mg concentrations. Furthermore, the tetragonal crystal structure is more stable, as Mg prefers the octahedral sites in this compound.

## Mg(Rh/Ir)<sub>2</sub>O<sub>4</sub>

We turn now to oxide spinels with  $4d$  and  $5d$  transition metals located in the B sites. These compounds often show a ferromagnetic ordering of the spins. The identical magnetic direction of the spins does not induce any distortion and the B-O bonds show no elongations or compressions. Electronically they are not Jahn-Teller active.

It should be noted that in spinel oxides, the B-O bonds are predominantly covalent. We have previously shown<sup>19</sup> that the migration barrier depends sensitively on the B-O bond length and the electronegativity difference between the B and O atoms.

We found a minimum in the height of the migration barriers for electronegativity difference values of  $\Delta\chi^2 \approx 2$ . Based on the identification of this pronounced minimum and the corresponding matching properties of Rh and Ir, we identify MgIr<sub>2</sub>O<sub>4</sub> as a super-ionic conductor with high Mg mobility with a migration barrier of only 0.319 eV, as shown in Fig. 6. Rh with a similar electronegativity as Ir also leads to a high Mg mobility in the spinel oxide framework with a migration barrier of only 0.429 eV (see Fig. 6).

The electronic structure of these two compounds is similar to each other. They are non-magnetic oxides, solely with trigonal distortions. The calculated DOS of MgRh<sub>2</sub>O<sub>4</sub>, Fig. 5 shows a filled valence band from -7.5 eV to -2.5 eV, dominantly of O- $p$  character, followed by Rh- $t_{2g}$  states from -2.5 to 0 eV. The bandgap originates from the crystal field splitting of the  $d$  orbitals of about 1 eV. The conduction band is made of empty  $e_g$  orbitals. This compound shows relatively small trigonal distortions compared to the other oxide spinels.

While the energy above *hull* of 0.287 eV/atom for MgIr<sub>2</sub>O<sub>4</sub> indicates instability of the spinel structure, the high stability of the MgRh<sub>2</sub>O<sub>4</sub> spinel oxide has been calculated through the energy above *hull* of 0.000 eV/atom. The calculated open-circuit voltages are 2.2 eV and 1.9 eV for the Rh and Ir spinels, respectively. Our calculations yield an increase of the open-circuit voltage for low Mg concentrations in both systems. Therefore, they are ideal candidates for cathode materials in Mg batteries with medium voltages.

Note that iridium and rhodium exhibit a low abundance in the earth's crust, making both

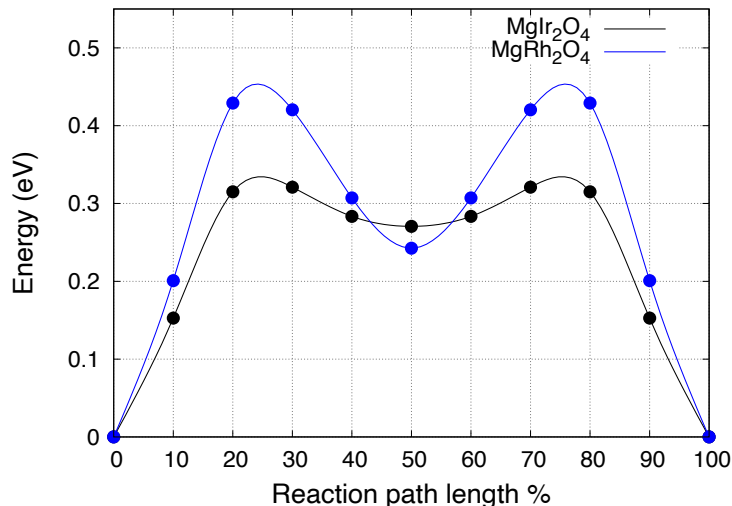


Figure 6: Mg migration energy barriers (in eV) as a function of the reaction path coordinate derived from periodic DFT calculations combined with NEB for the single-ion migration from tetrahedral site to the octahedral void and then to the next tetrahedral site corresponding to the  $\text{MgIr}_2\text{O}_4$  spinels with the black color and the  $\text{MgRh}_2\text{O}_4$  spinels with the blue color. The minimum energy is set to zero.

iridium and rhodium to expensive raw materials. Battery materials should be sustainable and associated with a high security of supply. However, there is always a compromise between gravimetric and volumetric energy density, abundance, cost and performance. Our calculations demonstrate that there are spinel oxides that promise a high Mg mobility as an electrode material. Possibly by doping less expensive oxide spinels with either iridium or rhodium a compromise between cost and performance can be achieved.

## Performance evaluation of the considered spinels

After having separately discussed the considered spinel materials, we now summarize the results with respect to the ion mobility, and in the following we do the same with respect to the electrochemical and structural properties of the oxide spinels.  $\text{Mn}_2\text{O}_4$  spinels have been successfully commercialized for use in Li-ion batteries. However, for this particular spinel, there is a high  $\text{Mg}^{2+}$  diffusion barrier of 0.67 eV, which is higher than the  $\text{Li}^+$  ion migration barriers in all  $\text{M}_2\text{O}_4$  ( $\text{M} = \text{Mn}, \text{Co}, \text{Ni}, \text{Cr}$ ) spinels which lie in the range 0.40-0.60 eV.

Among the considered  $3d$  transition metals, Fe (0.94 eV) and V (0.78 eV) have the highest barriers for  $\text{Mg}^{2+}$  ion diffusion, while Cr and Co are better conductors (0.51 eV). It should be noted that the migration barriers at low Mg concentrations are usually higher than those at high Mg concentrations. Thus, the Mg mobility becomes lower as the spinels change from the Mg-rich to the Mg-deficient limit.

Our calculations reveal that the tetrahedral sites are more stable for Mg than the octahedral sites for early transition metals in fully occupied Mg-spinels, while late transition metals such as Fe, Co, and Ni lead to a higher Mg stability in the octahedral sites.

Going from the  $3d$  transition metals to the  $4d$  and  $5d$  metals such as Rh and Ir, the migration barriers obtained for  $\text{Mg}^{2+}$  in these oxide spinels lie within 0.30-0.50 eV in the high Mg concentration limit. Accordingly, whereas  $\text{Li}^+$  intercalates easily into various spinel oxides,  $\text{Mg}^{2+}$  intercalation can benefit from more electronegative transition metals. Furthermore, these elements suppress the structural distortions coming from the antiferromagnetic order of the  $3d$ -orbitals. We also propose that investigating doped systems with two different transition metals might lead to the identification of further oxide spinel materials with favorable properties as cathode materials for Mg batteries.

An additional essential parameter for the performance of a battery system is the open-circuit voltage. After understanding the electronic and structural properties, we address the principles that determine the crucial properties of electrochemical cells, voltages, and capacities.

The open-circuit voltage,  $V_{OC}$ , is obtained through the Mg intercalation energy  $E_{inter}$  with respect to a metallic magnesium anode. In the Mg intercalation energy, the Gibbs free energy  $G$  is approximated by the total energy  $E$ , neglecting the influence of zero-point energies and entropic contributions at finite temperatures.

The calculated open-circuit voltages in the high magnesium concentrations indicate that the spinel oxides based on Cr, Mn, Fe, Co, and Ni exhibit high theoretical voltages for Mg intercalation. It should be noted that the voltages are referenced to the bulk metal phase of

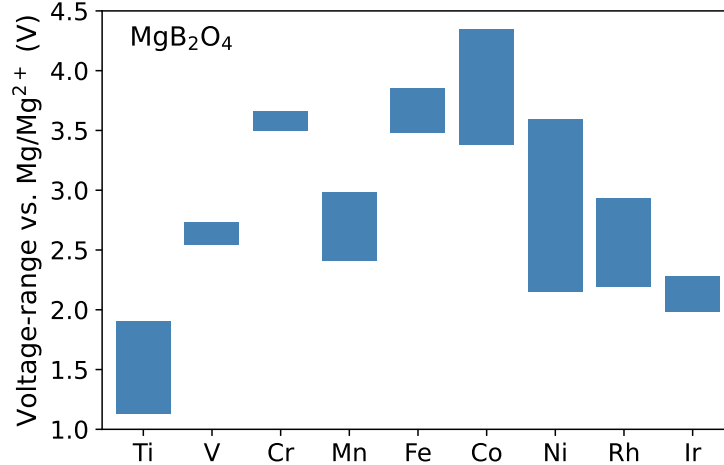


Figure 7: The calculated voltage range for oxide spinel compounds as a function of the redox-active transition metals. The voltage range is obtained as the range between the calculated voltages for the low and high Mg concentrations of the considered compounds.

Mg metal. The Mg-based spinel oxides exhibit lower potentials for Mg intercalation (less than 4 V) compared with Li spinels that operate at potentials for Li intercalation voltages 4 to 5 V. Except for Ti which has an Mg intercalation voltage lower than 2 V, most Mg intercalation potentials range between 2 and 4 V. However, the additional charge of the bivalent Mg<sup>2+</sup> causes a higher energy density in spinel cathodes compared to the monovalent Li<sup>+</sup>. Hence, the considered Mg oxide spinels are viable candidates from the point of view of theoretical capacity.

The maximum theoretical specific energy (MTSE) corresponding to the energy per unit weight is given by

$$\text{MTSE} = (xV/W_t)F \quad (5)$$

where  $W_t$  is the sum of the molecular weights of the reactants engaged in the intercalating reaction with a Mg concentration  $x$ , and  $V$  stands for the average voltage of this reaction.  $F$  is the Faraday constant.

Theoretically, most spinel oxides exhibit an average voltage of 2-4 V and correspondingly a high MTSE. Therefore, oxide spinels are currently the most promising candidates for high-

performance Mg battery cathodes.

It should be mentioned that in these materials cooperative Jahn–Teller distortions are the cause of volume contraction/expansion. In Tab. 2, we also listed the calculated volume change  $\Delta V/V$  upon Mg removal. Most of these materials exhibit volume contraction and expansion after demagnesiumation of less than 3.7 % compared to the structures full of  $\text{Mg}^{2+}$ . In the commercial  $\text{LiCoO}_2$  cathode for Li-ion batteries, the cell volume shrinks by about 5% after delithiation.<sup>50</sup> Therefore, the volume changes for magnesium intercalation are relatively low for oxide spinel cathodes, indicating a good cathode functionality with respect to volume change.

## Synthesizability of $\text{Ir}^{3+}$ and $\text{Rh}^{3+}$ substituted spinel compounds

Our calculations have demonstrated that  $\text{Mg}^{2+}$  spinel oxides including  $4d$  and  $5d$  transition metals have promising properties as cathode materials for Mg batteries, in particular also with regard to ion mobility. Nevertheless, the feasibility of synthesizing pure compounds as well as solid solutions under laboratory conditions needs to be guaranteed. Literature research confirms the synthesizability of  $\text{Rh}^{3+}$  containing spinel oxides as pure end-member compounds of Mg spinels like  $\text{MgRh}_2\text{O}_4$ <sup>51,52</sup> or in solid solutions like  $\text{Co}_{0.2}\text{Zn}_{0.8}\text{Fe}_{2-x}\text{Rh}_x\text{O}_4$ <sup>53</sup> or  $\text{CuCr}_{2-x}\text{Rh}_x\text{O}_4$ .<sup>54</sup> Therefore, a prosperous incorporation of  $\text{Rh}^{3+}$  in these compounds seems promising and should be subjected to further investigation to find prospective candidates for optimised ionic conductors in the field of Mg-oxide spinel compounds.

In contrast to Rh, the  $5d$  equivalent Iridium show a different behavior. Just few oxidic compounds with  $\text{Ir}^{3+}$ , like in layered  $\text{K}_{0.75}\text{Na}_{0.25}\text{IrO}_2$ ,<sup>55</sup> are reported, as most oxides show Ir in oxidation states  $\geq 4+$ . Miao and Seshadri have addressed this problem explaining it by relativistic effects.<sup>56</sup> These relativistic effects lead to a distinct stabilization in oxidation states between those typical for Rh and Ir oxides. In contrast to Rh, which is stable as sesquioxide, the iridates exhibit a higher stability in dioxides, or at lower chemical potentials a decomposition to Ir and  $\text{O}_2$  appear.



These results are confirmed by our lab experiments in which we investigated possible solid solutions in the  $\text{MgCr}_{2-x}\text{M}_x\text{O}_4$  (M: Rh, Ir) system. Different attempts to include  $\text{Ir}^{3+}$  in the Magnesiochromite lattice failed, leading to the formation of either  $\text{IrO}_2$  or Ir as second phases.

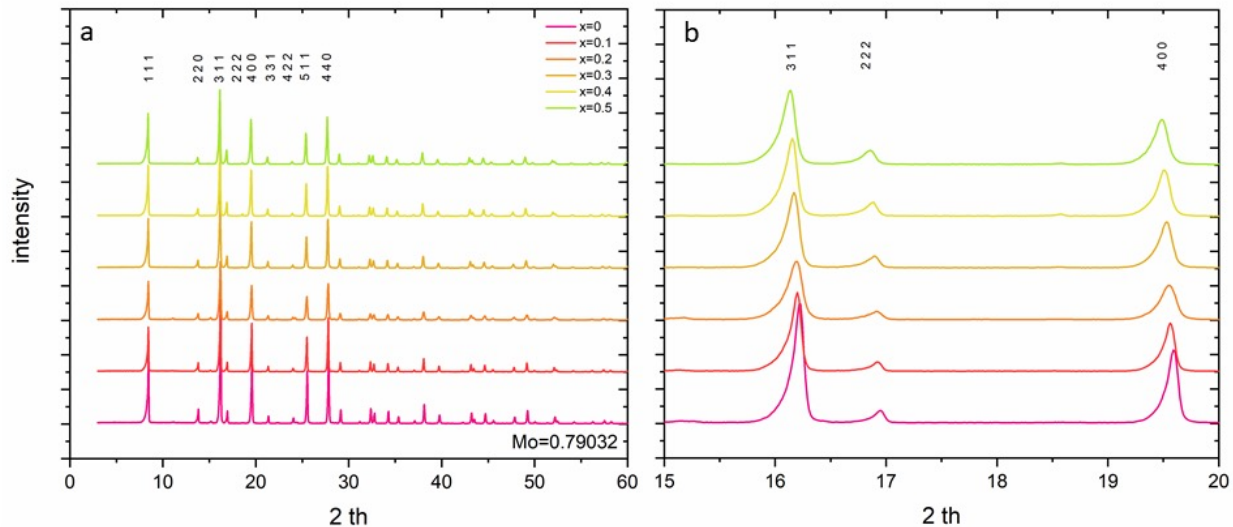


Figure 8: XRD patterns at room temperature for  $\text{MgCr}_{2-x}\text{Rh}_x\text{O}_4$  with  $x = 0-0.5$  (a) full pattern; (b) section from  $15-20^\circ$   $2\theta$  showing the shift of peak positions.

In contrast to that, initial results of our group suggest that the incorporation of  $\text{Rh}^{3+}$  into the Magnesiochromite lattice is possible. Samples with different amounts of rhodium have been synthesized by solid state reaction of  $\text{MgO}$  (ABCR 99,5%),  $\text{Cr}_2\text{O}_3$  (Strem 99%) and  $\text{Rh}_2\text{O}_3$  (Santa Cruz Biotechnology). Stoichiometric amounts of the oxides were mixed in an agate mortar in acetone. Afterward the mixture was pressed into pellets and calcinated in alumina boats in a muffle oven (Nabertherm) for one week at  $1000^\circ\text{C}$  with one intermediate grinding. The resulting brown powder was analysed by X-ray diffraction on a STOE StadiP diffractometer with monochromatic  $\text{MoK}\alpha_1$  radiation. The XRD patterns of compounds with Rh content of  $x = 0-0.5$  are depicted in Fig. 8a. An expected shift of the peak position can be clearly observed (Fig. 8b) as well as a continuous change in the intensities. Rietveld refinements were performed with Fullprof.<sup>57</sup> The results are given in Tab. 3 where the crystallographic information is listed.

Beside the main phase, small amounts of 0.2 – 4.2% of impurities are visible in the diffractograms. These consist of  $\text{Cr}_{2-x}\text{Rh}_x\text{O}_3$  and Rh. The lattice parameters follow Vegard’s law, with a small deviation (see Fig. 9). This sample shows the highest amount of impurity and differs by its color. In contrast to the others, this one is slightly green. The formation of a solid solution is therefore obvious, but must be investigated further, as well as the effects of the substitution on the physical properties. This will be part of a future work.

Table 3: Crystallographic information obtained by rietveld refinement.

$x_{Rh}$ by weight	Cell-parameter $a$ in Å	Thermal displacement parameter $u$ in Å <sup>2</sup>	Occupancy $\text{Occ}_{Rh}$	Impurities in wt%	Chi <sup>2</sup>
0.0	8.34376	0.38601	0	-	3.00
0.1	8.35497	0.38626	0.00416	1.0% $\text{Cr}_2\text{O}_3$	1.70
0.2	8.35589	0.38628	0.00248	4.2% $\text{Cr}_2\text{O}_3$	2.25
0.3	8.36755	0.38612	0.00539	0.2% Rh	2.00
0.4	8.37596	0.38605	0.01020	0.4% Rh	1.51
0.5	8.38555	0.38584	0.01316	0.3% Rh	1.80

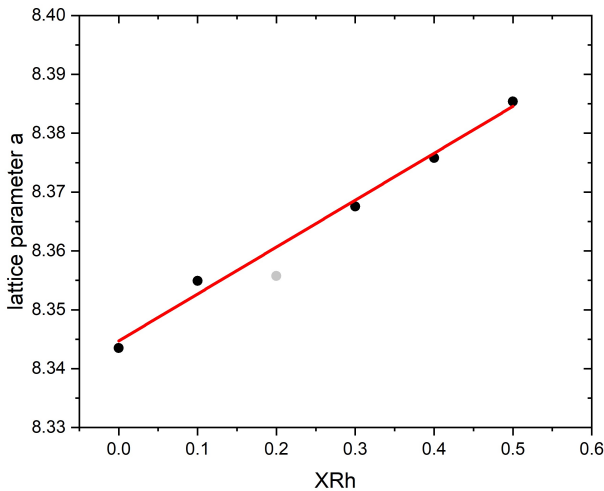


Figure 9: linear fit of lattice parameter with rising content of  $x_{Rh}$  (grey: excluded sample); standard deviation is indistinguishable from symbols.

## Conclusions and Summary

In this work, we have combined first-principles electronic structure calculations and experimental preparation efforts to identify promising oxide spinel materials for Mg battery cathodes with superior Mg mobility properties. According to our calculations, oxide spinels with the electronegative  $4d$  and  $5d$  transition metals Rh and Ir allow such superior transport properties together with an acceptable open circuit voltage with respect to a Mg metal anode. The specific non-magnetic electronic structure of these oxide spinels make the compounds rather stable showing only relatively small trigonal distortions. Furthermore, we performed first attempts to synthesize these materials obtaining promising results, in particular with respect to Ir compounds. In general, our results and the analysis based on a combined experimental and theoretical study provide a conceptual framework to understand fast ion conductivity in oxide spinel electrode materials that will also be beneficial for the understanding and improvement of ion mobility in other materials classes.

## Acknowledgements

This work contributes to the research performed at CELEST (Center for Electrochemical Energy Storage Ulm-Karlsruhe) and was funded by the German Research Foundation (DFG) under Project ID 390874152 (POLiS Cluster of Excellence) and the Dr. Barbara Mez-Starck foundation. The authors acknowledge computer time provided by the state of Baden-Württemberg through bwHPC and the German Research Foundation (DFG) through grant no INST 40/575-1 FUGG (JUSTUS 2 cluster).

## References

- (1) Hwang, J.-Y.; Myung, S.-T.; Sun, Y.-K. Sodium-ion batteries: present and future. *Chem. Soc. Rev.* **2017**, *46*, 3529–3614.

- (2) Yabuuchi, N.; Kubota, K.; Dahbi, M.; Komaba, S. Research Development on Sodium-Ion Batteries. *Chem. Rev.* **2014**, *114*, 11636–11682.
- (3) Gregory, T. D.; Hoffman, R. J.; Winterton, R. C. Nonaqueous Electrochemistry of Magnesium: Applications to Energy Storage. *J. Electrochem. Soc.* **1990**, *137*, 775–780.
- (4) Aurbach, D.; Lu, Z.; Schechter, A.; Gofer, Y.; Gizbar, H.; Turgeman, R.; Cohen, Y.; Moshkovich, M.; Levi, E. Prototype systems for rechargeable magnesium batteries. *Nature* **2000**, *407*, 724–727.
- (5) MacLaughlin, C. M. Status and Outlook for Magnesium Battery Technologies: A Conversation with Stan Whittingham and Sarbajit Banerjee. *ACS Energy Lett.* **2019**, *4*, 572–575.
- (6) Davidson, R. et al. Mapping mechanisms and growth regimes of magnesium electrodeposition at high current densities. *Mater. Horiz.* **2020**, *7*, 843–854.
- (7) Singh, N.; Arthur, T. S.; Ling, C.; Matsui, M.; Mizuno, F. A high energy-density tin anode for rechargeable magnesium-ion batteries. *Chem. Commun.* **2013**, *49*, 149–151.
- (8) Zhao-Karger, Z.; Gil Bardaji, M. E.; Fuhr, O.; Fichtner, M. A new class of non-corrosive, highly efficient electrolytes for rechargeable magnesium batteries. *J. Mater. Chem. A* **2017**, *5*, 10815–10820.
- (9) Sun, X.; Bonnick, P.; Duffort, V.; Liu, M.; Rong, Z.; Persson, K. A.; Ceder, G.; Nazar, L. F. A high capacity thiospinel cathode for Mg batteries. *Energy Environ. Sci.* **2016**, *9*, 2273–2277.
- (10) Canepa, P.; Sai Gautam, G.; Hannah, D. C.; Malik, R.; Liu, M.; Gallagher, K. G.; Persson, K. A.; Ceder, G. Odyssey of Multivalent Cathode Materials: Open Questions and Future Challenges. *Chem. Rev.* **2017**, *117*, 4287–4341.

- (11) Orikasa, Y.; Masese, T.; Koyama, Y.; Mori, T.; Hattori, M.; Yamamoto, K.; Okado, T.; Huang, Z.-D.; Minato, T.; Tassel, C.; Kim, J.; Kobayashi, Y.; Abe, T.; Kageyama, H.; Uchimoto, Y. High energy density rechargeable magnesium battery using earth-abundant and non-toxic elements. *Sci. Rep.* **2014**, *4*, 5622.
- (12) NuLi, Y.; Yang, J.; Wang, J.; Li, Y. Electrochemical Intercalation of  $Mg^{2+}$  in Magnesium Manganese Silicate and Its Application as High-Energy Rechargeable Magnesium Battery Cathode. *J. Phys. Chem. C* **2009**, *113*, 12594–12597.
- (13) Ling, C.; Mizuno, F. Phase Stability of Post-spinel Compound  $AMn_2O_4$  ( $A = Li, Na,$  or  $Mg$ ) and Its Application as a Rechargeable Battery Cathode. *Chem. Mater.* **2013**, *25*, 3062–3071.
- (14) Liu, M.; Rong, Z.; Malik, R.; Canepa, P.; Jain, A.; Ceder, G.; Persson, K. A. Spinel compounds as multivalent battery cathodes: a systematic evaluation based on ab initio calculations. *Energy Environ. Sci.* **2015**, *8*, 964–974.
- (15) Ling, C.; Zhang, R.; Arthur, T. S.; Mizuno, F. How General is the Conversion Reaction in Mg Battery Cathode: A Case Study of the Magnesiumation of  $\alpha$ - $MnO_2$ . *Chem. Mater.* **2015**, *27*, 5799–5807.
- (16) Kim, C.; Phillips, P. J.; Key, B.; Yi, T.; Nordlund, D.; Yu, Y.-S.; Bayliss, R. D.; Han, S.-D.; He, M.; Zhang, Z.; Burrell, A. K.; Klie, R. F.; Cabana, J. Direct Observation of Reversible Magnesium Ion Intercalation into a Spinel Oxide Host. *Adv. Mater.* **2015**, *27*, 3377–3384.
- (17) Dillenz, M.; Sotoudeh, M.; Euchner, H.; Groß, A. Screening of Charge Carrier Migration in the  $MgSc_2Se_4$  Spinel Structure. *Front. Energy Res.* **2020**, *8*, 260.
- (18) Sotoudeh, M.; Dillenz, M.; Groß, A. Mechanism of Magnesium Transport in Spinel Chalcogenides. *Adv. Energy Sustainability Res.* **2021**, *2*, 2100113.

- (19) Sotoudeh, M.; Groß, A. Descriptor and Scaling Relations for Ion Mobility in Crystalline Solids. *JACS Au* **2022**, *2*, 463–471.
- (20) Sotoudeh, M.; Groß, A. Stability of Magnesium Binary and Ternary Compounds for Batteries Determined from First Principles. *J. Phys. Chem. Lett.* **2022**, *13*, 10092–10100.
- (21) Bayliss, R. D.; Key, B.; Sai Gautam, G.; Canepa, P.; Kwon, B. J.; Lapidus, S. H.; Dogan, F.; Adil, A. A.; Lipton, A. S.; Baker, P. J.; Ceder, G.; Vaughey, J. T.; Cabana, J. Probing Mg Migration in Spinel Oxides. *Chem. Mater.* **2020**, *32*, 663–670.
- (22) Bachman, J. C.; Muy, S.; Grimaud, A.; Chang, H.-H.; Pour, N.; Lux, S. F.; Paschos, O.; Maglia, F.; Lupart, S.; Lamp, P.; Giordano, L.; Shao-Horn, Y. Inorganic Solid-State Electrolytes for Lithium Batteries: Mechanisms and Properties Governing Ion Conduction. *Chem. Rev.* **2016**, *116*, 140–162.
- (23) Yabuuchi, N.; Takeuchi, M.; Nakayama, M.; Shiiba, H.; Ogawa, M.; Nakayama, K.; Ohta, T.; Endo, D.; Ozaki, T.; Inamasu, T.; Sato, K.; Komaba, S. High-capacity electrode materials for rechargeable lithium batteries: Li<sub>3</sub>NbO<sub>4</sub>-based system with cation-disordered rocksalt structure. *Proc. Natl. Acad. Sci. U.S.A.* **2015**, *112*, 7650–7655.
- (24) Koettgen, J.; Bartel, C. J.; Ceder, G. Computational investigation of chalcogenide spinel conductors for all-solid-state Mg batteries. *Chem. Commun.* **2020**, *56*, 1952–1955.
- (25) Ben Yahia, M.; Vergnet, J.; Saubanère, M.; Doublet, M.-L. Unified picture of anionic redox in Li/Na-ion batteries. *Nat. Mater.* **2019**, *18*, 496–502.
- (26) Hohenberg, P.; Kohn, W. Inhomogeneous Electron Gas. *Phys. Rev.* **1964**, *136*, B864–B871.

- (27) Kohn, W.; Sham, L. J. Self-Consistent Equations Including Exchange and Correlation Effects. *Phys. Rev.* **1965**, *140*, A1133–A1138.
- (28) Euchner, H.; Groß, A. Atomistic modeling of Li- and post-Li-ion batteries. *Phys. Rev. Materials* **2022**, *6*, 040302.
- (29) Perdew, J. P.; Burke, K.; Ernzerhof, M. Generalized Gradient Approximation Made Simple. *Phys. Rev. Lett.* **1996**, *77*, 3865–3868.
- (30) Blöchl, P. E. Projector augmented-wave method. *Phys. Rev. B* **1994**, *50*, 17953–17979.
- (31) Kresse, G.; Hafner, J. Ab initio molecular dynamics for liquid metals. *Phys. Rev. B* **1993**, *47*, 558–561.
- (32) Kresse, G.; Furthmüller, J. Efficient iterative schemes for ab initio total-energy calculations using a plane-wave basis set. *Phys. Rev. B* **1996**, *54*, 11169–11186.
- (33) Kresse, G.; Joubert, D. From ultrasoft pseudopotentials to the projector augmented-wave method. *Phys. Rev. B* **1999**, *59*, 1758–1775.
- (34) Jepsen, O.; Anderson, O. K. The electronic structure of h.c.p. Ytterbium. *Solid State Commun.* **1971**, *9*, 1763–1767.
- (35) Lehmann, G.; Taut, M. On the Numerical Calculation of the Density of States and Related Properties. *Phys. Stat. Sol. (b)* **1972**, *54*, 469.
- (36) Blöchl, P. E.; Jepsen, O.; Andersen, O. K. Improved tetrahedron method for Brillouin-zone integrations. *Phys. Rev. B* **1994**, *49*, 16223–16233.
- (37) Dudarev, S. L.; Botton, G. A.; Savrasov, S. Y.; Humphreys, C. J.; Sutton, A. P. Electron-energy-loss spectra and the structural stability of nickel oxide: An LSDA+U study. *Phys. Rev. B* **1998**, *57*, 1505–1509.

- (38) Sheppard, D.; Terrell, R.; Henkelman, G. Optimization methods for finding minimum energy paths. *J. Chem. Phys.* **2008**, *128*, 134106.
- (39) Mehrer, H. *Diffusion in Solids: Fundamentals, Methods, Materials, Diffusion-Controlled Processes*; Springer Series in Solid-State Sciences; Springer Berlin Heidelberg, 2007.
- (40) Heyd, J.; Scuseria, G. E.; Ernzerhof, M. Hybrid functionals based on a screened Coulomb potential. *J. Chem. Phys.* **2003**, *118*, 8207–8215.
- (41) Bartel, C. J. Review of computational approaches to predict the thermodynamic stability of inorganic solids. *J. Mater. Sci.* **2022**, *57*, 10475–10498.
- (42) Jain, A.; Ong, S. P.; Hautier, G.; Chen, W.; Richards, W. D.; Dacek, S.; Cholia, S.; Gunter, D.; Skinner, D.; Ceder, G.; Persson, K. A. Commentary: The Materials Project: A materials genome approach to accelerating materials innovation. *APL Mater.* **2013**, *1*, 011002.
- (43) Wang, L.; Maxisch, T.; Ceder, G. Oxidation energies of transition metal oxides within the GGA + U framework. *Phys. Rev. B* **2006**, *73*, 195107.
- (44) Jain, A.; Hautier, G.; Ong, S. P.; Moore, C. J.; Fischer, C. C.; Persson, K. A.; Ceder, G. Formation enthalpies by mixing GGA and GGA + U calculations. *Phys. Rev. B* **2011**, *84*, 045115.
- (45) Burdett, J. K.; Price, G. D.; Price, S. L. Role of the crystal-field theory in determining the structures of spinels. *J. Am. Chem. Soc.* **1982**, *104*, 92–95.
- (46) Banerjee, S. K.; O'Reilly, W.; Gibb, T.; Greenwood, N. The behaviour of ferrous ions in iron-titanium spinels. *J. Phys. Chem. Sol.* **1967**, *28*, 1323 – 1335.
- (47) Sickafus, K. E.; Wills, J. M.; Grimes, N. W. Structure of Spinel. *J. Am. Ceram. Soc.* **1999**, *82*, 3279–3292.



- (48) Shannon, R. D. Revised effective ionic radii and systematic studies of interatomic distances in halides and chalcogenides. *Acta Cryst. A* **1976**, *32*, 751–767.
- (49) Lacroix, C.; Mendels, P.; Mila, F. *Introduction to Frustrated Magnetism: Materials, Experiments, Theory*; Springer Series in Solid-State Sciences; Springer Berlin Heidelberg, 2011.
- (50) Wang, X.; Sone, Y.; Segami, G.; Naito, H.; Yamada, C.; Kibe, K. Understanding Volume Change in Lithium-Ion Cells during Charging and Discharging Using In Situ Measurements. *J. Electrochem. Soc.* **2007**, *154*, A14.
- (51) Capobianco, C. J. On the thermal decomposition of  $\text{MgRh}_2\text{O}_4$  spinel and the solid solution  $\text{Mg}(\text{Rh}, \text{Al})_2\text{O}_4$ . *Thermochim. Acta* **1993**, *220*, 7–16.
- (52) Nell, J.; O’Neill, H. S. The Gibbs free energy of formation and heat capacity of  $\beta$ - $\text{Rh}_2\text{O}_3$  and  $\text{MgRh}_2\text{O}_4$ , the MgO-Rh-O phase diagram, and constraints on the stability of  $\text{Mg}_2\text{Rh}^{4+}\text{O}_4$ . *Geochim. Cosmochim. Acta* **1997**, *61*, 4159–4171.
- (53) Bhowmik, R.; Ranganathan, R. Cluster glass behaviour in  $\text{Co}_{0.2}\text{Zn}_{0.8}\text{Fe}_{2-x}\text{Rh}_x\text{O}_4$  ( $x=0-1.0$ ). *J. Magn. Magn. Mater.* **2001**, *237*, 27–40.
- (54) Padmanaban, N.; Avasthi, B.; Ghose, J. Solid state studies on rhodium-substituted  $\text{CuCr}_2\text{O}_4$  spinel oxide. *J. Solid State Chem.* **1990**, *86*, 286–292.
- (55) Weber, D.; Schoop, L. M.; Wurmbrand, D.; Nuss, J.; Seibel, E. M.; Tafti, F. F.; Ji, H.; Cava, R. J.; Dinnebier, R. E.; Lotsch, B. V. Trivalent Iridium Oxides: Layered Triangular Lattice Iridate  $\text{K}_{0.75}\text{Na}_{0.25}\text{IrO}_2$  and Oxyhydroxide  $\text{IrOOH}$ . *Chem. Mater.* **2017**, *29*, 8338–8345.
- (56) Miao, M.-S.; Seshadri, R.  $\text{Rh}_2\text{O}_3$  versus  $\text{IrO}_2$ : relativistic effects and the stability of  $\text{Ir}^{4+}$ . *J. Phys. Condens. Matter* **2012**, *24*, 215503.

- (57) Roisnel, T.; Rodríguez-Carvajal, J. WinPLOTTR: A Windows Tool for Powder Diffraction Pattern Analysis. *European Powder Diffraction EPDIC 7*. 2001; pp 118–123.